

High-pressure strengthening in ultrafine-grained metals

<https://doi.org/10.1038/s41586-020-2036-z>

Received: 20 January 2019

Accepted: 3 December 2019

Published online: 24 February 2020

 Check for updates

Xiaoling Zhou^{1,2,3,14}, Zongqiang Feng^{4,14}, Linli Zhu^{5,6,14}, Jianing Xu^{1,7,14}, Lowell Miyagi³, Hongliang Dong¹, Hongwei Sheng¹, Yanju Wang¹, Quan Li^{8,9,10}, Yanming Ma^{8,9,10}, Hengzhong Zhang¹, Jinyuan Yan², Nobumichi Tamura², Martin Kunz², Katie Lutker¹¹, Tianlin Huang¹², Darcy A. Hughes¹³, Xiaoxu Huang⁴ & Bin Chen¹✉

HPSTAR
905-2020

The Hall–Petch relationship, according to which the strength of a metal increases as the grain size decreases, has been reported to break down at a critical grain size of around 10 to 15 nanometres^{1,2}. As the grain size decreases beyond this point, the dominant mechanism of deformation switches from a dislocation-mediated process to grain boundary sliding, leading to material softening. In one previous approach, stabilization of grain boundaries through relaxation and molybdenum segregation was used to prevent this softening effect in nickel–molybdenum alloys with grain sizes below 10 nanometres³. Here we track in situ the yield stress and deformation texturing of pure nickel samples of various average grain sizes using a diamond anvil cell coupled with radial X-ray diffraction. Our high-pressure experiments reveal continuous strengthening in samples with grain sizes from 200 nanometres down to 3 nanometres, with the strengthening enhanced (rather than reduced) at grain sizes smaller than 20 nanometres. We achieve a yield strength of approximately 4.2 gigapascals in our 3-nanometre-grain-size samples, ten times stronger than that of a commercial nickel material. A maximum flow stress of 10.2 gigapascals is obtained in nickel of grain size 3 nanometres for the pressure range studied here. We see similar patterns of compression strengthening in gold and palladium samples down to the smallest grain sizes. Simulations and transmission electron microscopy reveal that the high strength observed in nickel of grain size 3 nanometres is caused by the superposition of strengthening mechanisms: both partial and full dislocation hardening plus suppression of grain boundary plasticity. These insights contribute to the ongoing search for ultrastrong metals via materials engineering.

Understanding the strengthening of nanograined metals has been puzzling, as mixed results of both size softening and hardening have been reported^{4–7}. The main challenges in resolving this debate are the difficulty in synthesizing high-quality, ultrafine-grained metal samples for traditional tension or hardness tests and making statistically reproducible measurements. Some researchers have pointed out that reported size softening may be related to the preparation of materials⁸. Porosity, amorphous regions and impurities may be introduced during sample preparation by methods such as inert gas condensation and electrodeposition, leading to softening in micro-hardness measurements and tension tests. Another difficulty is identifying the dominant plastic deformation mechanisms of nanograined metals. Various defects or processes at the nanoscale have been reported,

including dislocations^{9,10}, deformation twinning^{11,12}, stacking faults¹¹, grain boundary (GB) migration¹³, GB sliding¹ and grain rotation^{14,15}. Hence, the processes that dominate plastic deformation and thus determine the strength of nanograined metals are still unclear.

In this study, we use radial diamond anvil cell (DAC) X-ray diffraction (XRD) techniques to track in situ the yield stress and deformation texturing of nickel of various grain sizes. We find that mechanical strengthening can be extended down to a grain size of 3 nm (the smallest we have available), which is much smaller than the previously reported strongest sizes of nanograined metals. This finding pushes mechanical strengthening to the lowest recorded grain size (to our knowledge), demonstrating the potential for achieving ultrahigh strengths in metals.

¹Center for High Pressure Science and Technology Advanced Research, Pudong, Shanghai, China. ²Advanced Light Source, Lawrence Berkeley National Laboratory, Berkeley, CA, USA.

³Department of Geology and Geophysics, University of Utah, Salt Lake City, UT, USA. ⁴International Joint Laboratory for Light Alloys (MOE), College of Materials Science and Engineering, Chongqing University, Chongqing, China. ⁵Center for X-Mechanics, Zhejiang University, Hangzhou, China. ⁶Key Laboratory of Soft Machines and Smart Devices of Zhejiang Province, School of Aeronautics and Astronautics, Zhejiang University, Hangzhou, China. ⁷Department of Physics, Fudan University, Shanghai, China. ⁸State Key Lab of Superhard Materials, College of Physics, Jilin University, Changchun, China. ⁹International Center for Computational Method and Software, College of Physics, Jilin University, Changchun, China. ¹⁰International Center for Future Science, Jilin University, Changchun, China. ¹¹Department of Chemistry, University of California, Berkeley, CA, USA. ¹²Shenyang National Laboratory for Materials Science, Chongqing University, Chongqing, China. ¹³Unaffiliated, Fremont, CA, USA. ¹⁴These authors contributed equally: Xiaoling Zhou, Zongqiang Feng, Linli Zhu, Jianing Xu. ✉e-mail: xiaoxu@hpstar.ac.cn

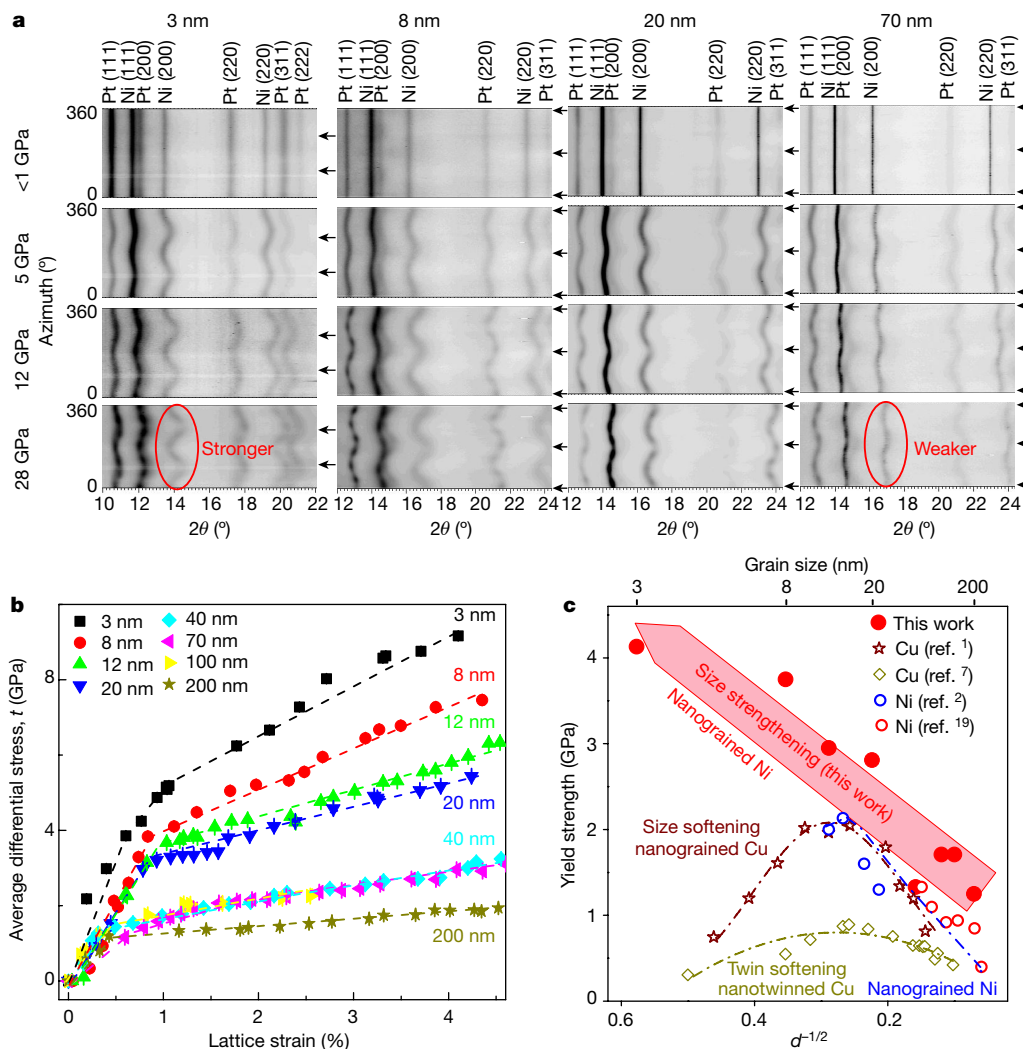


Fig. 1 | Size strengthening of nanograined nickel. **a**, Azimuthally (0–360°) unrolled diffraction images of nickel at different pressures. The black arrows indicate the axial compression direction. Each measurement is repeated at least two times. **b**, Differential stress versus the lattice strain of nickel (see Supplementary Information). We note that for some of the data points the error bars (standard deviations; see equations (6)–(9) and Supplementary Information) are smaller than the sizes of symbols. **c**, Extrapolated yield strength of nickel at ambient conditions without GB sliding (from EVPSC

simulations) versus grain size. The yield strength of nanograined Cu is obtained from molecular dynamics simulations (ref. ¹) and experimental data of nanotwinned Cu (ref. ⁷) and nanograined Ni (refs. ^{2,19}). The yield strength value of nickel in ref. ² is taken as one-third of its hardness. For nanotwinned Cu, d represents the twin thickness. The inverse Hall–Petch effect has been reported for both Cu (refs. ^{1,7}) and Ni (ref. ²). The smallest grain size of nickel in the study of ref. ² is 12 nm.

Radial DAC XRD experiments (Extended Data Fig. 1, see Supplementary Information) were performed at beamline 12.2.2 at the Advanced Light Source, Lawrence Berkeley National Laboratory, and at the Shanghai Synchrotron Radiation Facility. Eight nickel samples with particle (grain) sizes ranging from 3 nm to 200 nm (Extended Data Figs. 2, 3) were measured. The relatively narrow size distributions allow for the investigation of the size dependence of the material's strength. In a sample under uniaxial compression, the stress can be separated into hydrostatic and deviatoric stress components. The differential stress between the maximum and minimum compression directions can be obtained using deviatoric strain theory¹⁶ (see Supplementary Information). The measured XRD peak positions provide information on differential strains as well as differential stresses (Fig. 1a). Plastic deformation has an influence on deviatoric strains measured using diffraction, and so the differential strain/stress measured with radial DAC XRD can capture the transition from elastic- to plastic-deformation-dominant behaviours and can provide information on yield strength, strain hardening and so on (Fig. 1 and Extended Data Fig. 4). At the same pressure, the

differential strain of the 3-nm-grain-sized nickel is higher than that of larger-grained counterparts. The larger curvatures (the ellipticity of the XRD rings, which translates into nonlinearity of the lines plotted along the azimuth angle) of diffraction lines for smaller nanocrystals indicate higher elastic deformation and the greater ability of the material to support differential stress in the crystal plane without plastic deformation. We used Rietveld refinement implemented in the MAUD software¹⁷ to analyse the differential strain and texture of our samples at each pressure. The average differential stress of nickel versus its lattice strain can thus be obtained (Fig. 1b) using equations (5) to (9) (see Supplementary Information). To remove the effect of hardening induced by hydrostatic pressure, we performed elasto-viscoplastic self-consistent (EVPSC)¹⁸ simulations (see Supplementary Information) to simulate the stress-strain curves of nickel under ambient conditions (Extended Data Fig. 5). This enables the comparison of our extrapolated strength results at zero pressure with those of conventional tests^{2,19} (Fig. 1c). The stress-strain curves (Fig. 1b and Extended Data Fig. 5c) show that instead of softening, smaller-grained nickel was stronger than its coarser counterparts, in

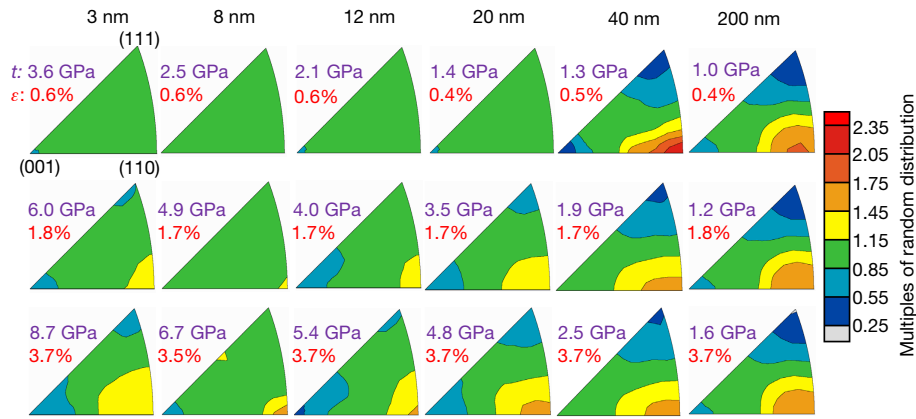


Fig. 2 | Inverse pole figures for the texture evolution of nickel with various grain sizes. Inverse pole figures show the probability of finding the pole to lattice plane in the compression direction. We note that no starting texture exists in all raw (uncompressed powder) samples. t and ϵ represent differential

stress and lattice strain, respectively. Texture strength is expressed as multiples of random distribution, for which 1 denotes a random distribution and a higher number represents a stronger texture.

strong contrast to the results of previous studies (Fig. 1c). The stress–strain curves of nanograined nickel also show a larger slope/hardening exponent (Fig. 1b), possibly owing to the increased plastic anisotropy in this smaller grain size (Extended Data Fig. 5). We note that a slight strength drop occurs in 40-nm-grain-sized nickel in EVPSC simulations; the cause remains to be further investigated.

The development of in situ deformation textures for nanograined nickel with various grain sizes was captured at different strains. As shown in Fig. 2, nickel samples with larger grain sizes above 20 nm show very strong deformation textures even at low strain. Nanograined nickel samples with grain sizes below 20 nm exhibit very weak deformation textures, indicating that traditional full dislocation activity becomes less active, whereas the strength increases with decreasing grain size. Meanwhile, all of the nickel samples develop a deformation texture, indicating that deformation mechanisms may still be based on dislocation slip and twin formation, since GB-mediated mechanisms would maintain the initial random textures.

Previous simulations^{1,20,21} have suggested that GB deformation plays a decisive part in the deformation mechanisms of sub-10-nm-grain-sized nanomaterials. Those studies proposed that size softening would occur as a result of the transition from dislocation-mediated to GB-mediated mechanisms. In our experiments, however, we observed no size softening but only size strengthening. The uniaxial compressional stress comprises hydrostatic and deviatoric stress components. The shear stress arising from the deviatoric stress could potentially activate GB mechanisms, whereas the hydrostatic stress of the compression increases the critical shear stress for GB migration and sliding, thereby suppressing those mechanisms; see equation (15).

To explore the mechanisms for continuous size strengthening, we simulated the critical stress for activating full and partial dislocations and for activating GB deformation (GB sliding and migration) in nanograined nickel. As shown in Fig. 3a, full dislocations are activated preferentially and are more dominant than partial dislocations above the critical grain size d_c^1 . The dislocation-dominant deformation shifts to GB-dominant deformation for grain sizes below a critical grain size d_c^2 . However, compression has a remarkable effect on this shift. The critical stress for activating GB deformation increases with pressure, resulting in the critical grain size d_c^2 being highly pressure-dependent. For example, the critical grain size for active GB deformation of nickel at >1 GPa is <2 nm (Fig. 3b); this suggests that almost no GB deformation is activated in our experiments because hydrostatic pressure is higher than 1 GPa, that is, the GB-deformation associated softening of nanograins has been greatly inhibited during compression. Consequently, when GB-associated deformation (extrinsic deformation) is

suppressed, the material strength should be determined mainly by intrinsic deformation properties, which are associated with lattice strain and defects in the interiors of grains.

It is known that the critical stress to activate dislocations increases with decreasing grain size. In a simplified analytical dislocation model that considers partial dislocations emitted from GBs of nanograins, the critical stress for emitting a full and partial dislocation²² can be described as:

$$\tau_f = \frac{Gb_f}{d} \quad (1)$$

$$\tau_p = \frac{Gb_p}{3d} + (1 - \delta) \frac{\gamma}{Gb_p} \quad (2)$$

where b_f and b_p are the Burgers vectors of the full and partial dislocations, respectively; G is the shear modulus; γ is the stacking fault energy; and δ is the ratio of equilibrium stacking fault width to grain size. The critical stresses for nucleating both full and partial dislocations increase sharply as the grain size decreases towards the lower limit (Fig. 3a). This leads to the increase of yield strength at small grain size. Furthermore, partial dislocations are preferentially activated and overtake full dislocations below a critical grain size.

We studied the deformation behaviour of nanograined nickel by molecular dynamics simulations²³ (Fig. 3d). Two types of planar defects associated with partial dislocations (that is, nanotwins and stacking faults) as well as full dislocations are found in nanograined nickel under compression. To explore the deformation mechanisms, we conducted transmission electron microscopy (TEM) characterization on the recovered samples. As expected, high densities of full dislocations are seen in the coarse-grained sample (Fig. 4d). Remarkably, full dislocations are prevalent at all average grain sizes including the finest at 3 nm (Fig. 4a–c), although for the 3-nm-grain-sized sample the dislocations were observed in grains with slightly larger sizes than average. A detailed analysis of the four dislocations observed in the lower part of Fig. 4a is shown in the sketch in Fig. 4b based on the Thompson tetrahedron. Each of these dislocations is an extended dislocation composed of a stacking fault and two partial dislocations lying on $\{111\}$ slip planes. A Lomer–Cottrell lock and a stair rod are formed from the reactions of partial dislocations associated with the upper three dislocations, with the stair rod lying on a $\{100\}$ plane. These reaction products are immobile and thus provide a strong strengthening effect. A rough estimate of the density of full dislocations based on the dislocations in Fig. 4a suggests a density of about 10^{16} m^{-2} , which provides a strong

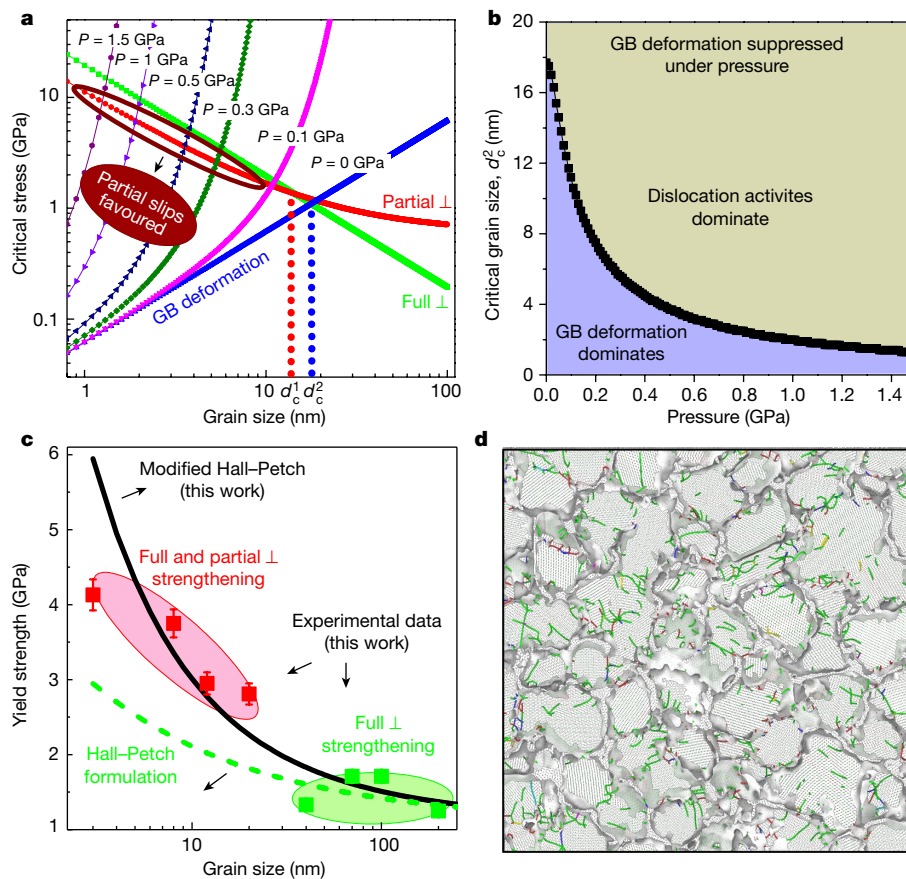


Fig. 3 | Computational simulation results and the modified Hall-Petch relationship. **a**, Comparison of simulated grain-size-dependent critical stresses for activating dislocations and GB deformation in nanograined nickel at different pressures. The \perp symbol represents a dislocation. **b**, Critical grain size d_c^2 as a function of pressure. **c**, The predicted yield strength compared with the experimental data for nanograined nickel. **d**, Classic molecular dynamics

simulation of 3-nm-grain-sized Ni compressed with 10% volume strain. Green indicates partial dislocations associated with stacking faults, twins and grain boundaries. Blue indicates perfect dislocations. Yellow, purple and red indicate a few $1/3\langle 001 \rangle$ (Hirth), $1/6\langle 110 \rangle$ (stair-rod) and other types of dislocations.

strengthening component for the flow stress. At the finest grain sizes, nanotwins form bounded by stacking faults, creating important new additions to the deformed structure. These nanotwins further refine the nanostructure and contribute to boundary strengthening by constraining dislocation motion. Steps in the twin boundaries are observed, forming incoherent twin boundaries that contain partial dislocations (Fig. 4). We note that the simultaneous and cooperative activation of different Shockley partial dislocations on parallel and neighbouring glide planes may be responsible for these twins²⁴. Stacking faults may expand under high stress, increasing their energy and making it favourable to form low-energy twins²⁵. Fivefold symmetry twins are also seen in both 3-nm-grain-sized and 20-nm-grain-sized quenched nickel samples (Fig. 4). Fivefold twins may pre-exist in the particles or form by the successive emission of partial dislocations from incoherent twin boundaries with high energy. The non-parallel twin boundaries give rise to strong overlapping of associated lattice strain fields, resulting in higher yield strength compared to those without fivefold twinned structures²⁶. This result is consistent with our observations in the mechanical measurements (Fig. 1b). In short, twinning and stacking faults observed in our TEM measurements originate from the nucleation and motion of partial dislocations. This provides compelling evidence that in the sub-20-nm regime of grain size, full-dislocation-mediated deformation shifts to both full and partial dislocations combined with deformation twinning.

Our strength measurements (Fig. 1b), computational simulations (Fig. 3a, c) and TEM observations (Fig. 4) indicate that a critical grain

size (around 20 nm) exists and corresponds to the shift in deformation mechanisms from full dislocation to full plus partial dislocation mediated deformation. This does not generate a maximum strength at the critical grain size but starts a stronger mode for strengthening. Notably, as shown in Fig. 4, the twins in 20 nm or smaller nickel grains are usually only several nanometres thick, but unlike growth twins, no softening is induced in pressurized nickel nanograins. Instead, size strengthening of nickel is even more pronounced in the smaller size range of nanograins. As shown in Fig. 3c, for grain sizes below 20 nm the measured yield strength of nanograined nickel largely deviates from the trend predicted by the traditional Hall-Petch model. Considering that the contribution of partial dislocations becomes important in fine nanograins, we propose a modified Hall-Petch relationship as follows:

$$\sigma_y = \sigma_0 + \frac{k_0}{\sqrt{d}} + \frac{k_1}{d} \quad (3)$$

where σ_y and d represent the yield strength and grain size, respectively, and σ_0 , k_0 and k_1 are constants. The first two terms represent the friction stress and Hall-Petch formulation associated with full dislocation boundary interaction. The third term is related to the partial dislocation contribution to yielding, which is inversely proportional to grain size d according to equation (2). The fitting of our experimental data with equation (3) shows that this new model reflects the effects of both full and partial dislocations, and can describe the size strengthening of

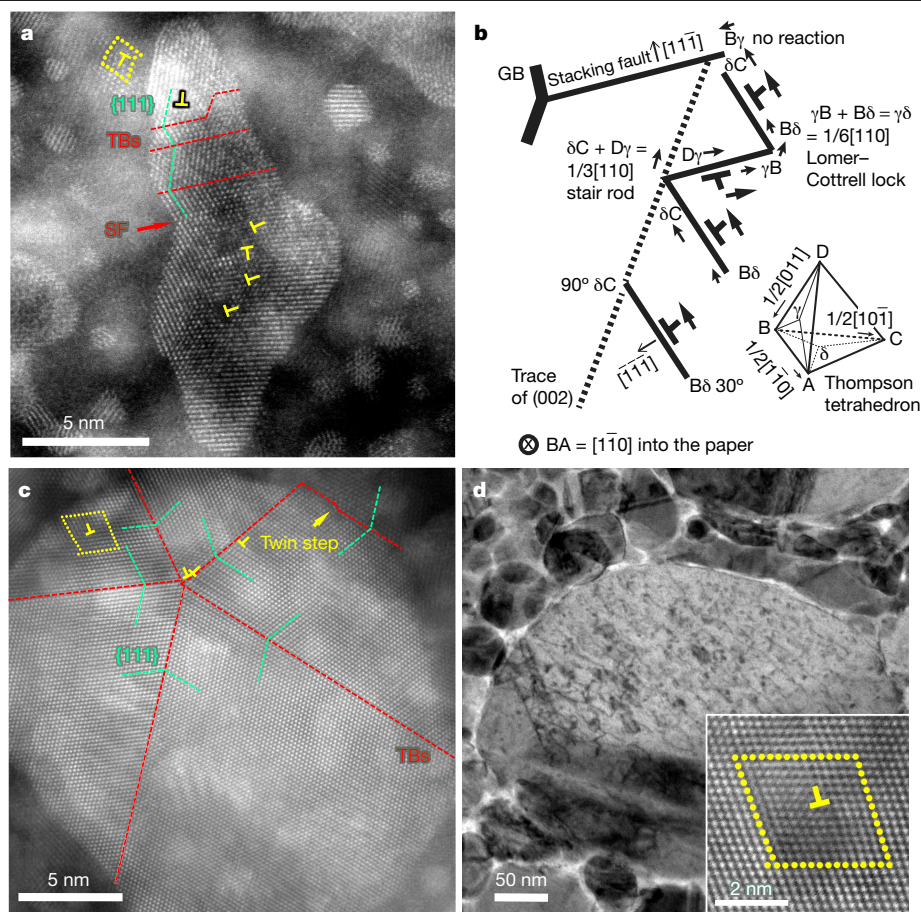


Fig. 4 | TEM examinations of nickel samples quenched from 40 GPa of three grain sizes. a, 3 nm; c, 20 nm; and d, 200 nm. Panel b is a sketch showing the analysis of dislocations observed in the lower part of the middle grain in panel a. We note the reactions of partial dislocations forming Lomer–Cottrell locks

metals over a wide size range. We note that this fit gives a high friction stress of about 1.1 GPa, k_1 of 9 MPa μm and a low k_0 of 101 MPa $\mu\text{m}^{1/2}$ compared to conventionally deformed Ni with 20 MPa and 158 MPa $\mu\text{m}^{1/2}$, respectively^{27,28}. To check the generality of the size strengthening for nanograined metals, we conducted similar high-pressure deformation experiments on nanograined gold and palladium. A similar enhanced strengthening effect at the lowest grain sizes was observed, which indicates that this full plus partial dislocation-mediated strengthening is common in compressed nanograined metals.

This size strengthening effect may apply not only to high-pressure cases but also provide guidance for applications at ambient conditions. A recent study³ reported that a twofold increase in hardness was achieved in nanograined Ni–Mo alloys by stabilizing GBs through Mo segregation. By using this technique yield strengths of around 1.6 GPa and 3.8 GPa were achieved in Ni and Ni–Mo alloys, respectively. In our experiments, an ultrahigh strength of about 4.2 GPa is achieved in pure nickel grains. This result suggests that compression is an effective method of suppressing GB sliding and migration in order to achieve ultrahigh strength.

This is also supported by the observation that the measured strength of coarse nickel in our compression test is higher than in conventional tension tests^{2,19}. In real applications, materials could be under either tension or compression. Tension tests are common in traditional mechanical characterization. However, evaluation of strength by tensile loading is often technically difficult for nanograined metals especially for sub-10-nm grain sizes. Compressive strength measurements using radial DAC XRD enables study of the mechanical properties of even

and a stair rod. Stacking faults (SFs), twin boundaries (TBs) and a few full dislocations can be found in 3 and 20 nm nickel samples. A high density of full dislocations is observed in the 200 nm nickel grains. The inset to **d** shows a high-resolution image of a full dislocation.

sub-10-nm-sized metals. In this synchrotron-based study, deformation behaviour and yield strength are obtained from the lattice changes of a large quantity of nanograins and exhibit reproducible trends in strength and grain size. Additionally, extrinsic factors like impurities and amorphous regions that may be introduced during conventional sample preparation could strongly affect the mechanical behaviour of nanograined metals. In our method, the strength in pure nickel grains is determined by the internal piezometer of crystalline lattice strain, which mitigates the effects of extrinsic factors.

Experimental work also indicates that partial-dislocation-associated mechanisms improve the thermal stability of grain boundaries of nanograins²⁹. If the grain boundaries of nanograined metals are sintered without grain coarsening, for example, through severe plastic deformation or explosive shock annealing³⁰, large pieces of nanograined metals with ultrahigh strength could potentially be fabricated for mass applications. In summary, achieving an ultrahigh strength in pure nickel through grain refinement and suppression of GB plasticity provides a new strategy for designing ultrastrong, ultrahard metals for future applications.

Online content

Any methods, additional references, Nature Research reporting summaries, source data, extended data, supplementary information, acknowledgements, peer review information; details of author contributions and competing interests; and statements of data and code availability are available at <https://doi.org/10.1038/s41586-020-2036-z>.

1. Schiøtz, J. & Jacobsen, K. W. A maximum in the strength of nanocrystalline copper. *Science* **301**, 1357–1359 (2003).
2. Schuh, C., Nieh, T. & Yamasaki, T. Hall–Petch breakdown manifested in abrasive wear resistance of nanocrystalline nickel. *Scr. Mater.* **46**, 735–740 (2002).
3. Hu, J., Shi, Y. N., Sauvage, X., Sha, G. & Lu, K. Grain boundary stability governs hardening and softening in extremely fine nanograined metals. *Science* **355**, 1292–1296 (2017).
4. Knapp, J. & Follstaedt, D. Hall–Petch relationship in pulsed-laser deposited nickel films. *J. Mater. Res.* **19**, 218–227 (2004).
5. Meyers, M. A., Mishra, A. & Benson, D. J. Mechanical properties of nanocrystalline materials. *Prog. Mater. Sci.* **51**, 427–556 (2006).
6. Huang, X., Hansen, N. & Tsuji, N. Hardening by annealing and softening by deformation in nanostructured metals. *Science* **312**, 249–251 (2006).
7. Lu, L., Chen, X., Huang, X. & Lu, K. Revealing the maximum strength in nanotwinned copper. *Science* **323**, 607–610 (2009).
8. Koch, C. C. & Narayan, J. The Inverse Hall–Petch Effect—Fact or Artifact? *MRS Online Proc. Lib. Arch.* **634**, B5.11, <https://www.cambridge.org/core/journals/mrs-online-proceedings-library-archive/article/inverse-hall-etch-effect-fact-or-artifact/E7759F8A3266F51367E3A87EFE13FA2B> (2000).
9. Chen, B. et al. Texture of nanocrystalline nickel: probing the lower size limit of dislocation activity. *Science* **338**, 1448–1451 (2012).
10. Hughes, D. & Hansen, N. Exploring the limit of dislocation based plasticity in nanostructured metals. *Phys. Rev. Lett.* **112**, 135504 (2014).
11. Chen, M. et al. Deformation twinning in nanocrystalline aluminum. *Science* **300**, 1275–1277 (2003).
12. Yamakov, V., Wolf, D., Phillpot, S. R., Mukherjee, A. K. & Gleiter, H. Dislocation processes in the deformation of nanocrystalline aluminium by molecular-dynamics simulation. *Nat. Mater.* **1**, 45–49 (2002).
13. Shan, Z. et al. Grain boundary-mediated plasticity in nanocrystalline nickel. *Science* **305**, 654–657 (2004).
14. Zhou, X. et al. Reversal in the size dependence of grain rotation. *Phys. Rev. Lett.* **118**, 096101 (2017).
15. Chen, B., Zhu, L., Xin, Y. & Lei, J. Grain rotation in plastic deformation. *Quantum Beam Sci.* **3**, 17 (2019).
16. Singh, A. K., Balasingh, C., Mao, H.-k., Hemley, R. J. & Shu, J. Analysis of lattice strains measured under nonhydrostatic pressure. *J. Appl. Phys.* **83**, 7567 (1998).
17. Lutterotti, L., Vasin, R. & Wenk, H.-R. Rietveld texture analysis from synchrotron diffraction images. I. Calibration and basic analysis. *Powder Diffr.* **29**, 76–84 (2014).
18. Wang, H., Wu, P., Tomé, C. & Huang, Y. A finite strain elastic–viscoplastic self-consistent model for polycrystalline materials. *J. Mech. Phys. Solids* **58**, 594–612 (2010).
19. Ebrahimi, F., Bourne, G., Kelly, M. S. & Matthews, T. Mechanical properties of nanocrystalline nickel produced by electrodeposition. *Nanostruct. Mater.* **11**, 343–350 (1999).
20. Yamakov, V., Wolf, D., Phillpot, S., Mukherjee, A. & Gleiter, H. Deformation-mechanism map for nanocrystalline metals by molecular-dynamics simulation. *Nat. Mater.* **3**, 43 (2004).
21. Van Swygenhoven, H., Derlet, P. & Frøseth, A. Stacking fault energies and slip in nanocrystalline metals. *Nat. Mater.* **3**, 399–403 (2004).
22. Zhu, Y., Liao, X. & Wu, X. Deformation twinning in nanocrystalline materials. *Prog. Mater. Sci.* **57**, 1–62 (2012).
23. Zepeda-Ruiz, L. A., Stukowski, A., Oettel, T. & Bulatov, V. V. Probing the limits of metal plasticity with molecular dynamics simulations. *Nature* **550**, 492–495 (2017).
24. Li, B., Li, B., Wang, Y., Sui, M. & Ma, E. Twinning mechanism via synchronized activation of partial dislocations in face-centered-cubic materials. *Scr. Mater.* **64**, 852–855 (2011).
25. Wang, J. & Huang, H. Shockley partial dislocations to twin: another formation mechanism and generic driving force. *Appl. Phys. Lett.* **85**, 5983–5985 (2004).
26. Zhang, Z., Huang, S., Chen, L., Zhu, Z. & Guo, D. Formation mechanism of fivefold deformation twins in a face-centered cubic alloy. *Sci. Rep.* **7**, 45405 (2017).
27. Thompson, A. A. W. Yielding in nickel as a function of grain or cell size. *Acta Metall.* **23**, 1337–1342 (1975).
28. Hughes, D. & Hansen, N. The microstructural origin of work hardening stages. *Acta Mater.* **148**, 374–383 (2018).
29. Huang, Q. et al. Nanotwinned diamond with unprecedented hardness and stability. *Nature* **510**, 250–253 (2014).
30. Zheng, S. et al. High-strength and thermally stable bulk nanolayered composites due to twin-induced interfaces. *Nat. Commun.* **4**, 1696 (2013).

Publisher's note Springer Nature remains neutral with regard to jurisdictional claims in published maps and institutional affiliations.

© The Author(s), under exclusive licence to Springer Nature Limited 2020

Data availability

The data that support the findings of this study are available from the corresponding authors upon reasonable request.

Acknowledgements We thank K. Lu, D. J. Jensen, N. Hansen, S.-I. Karato, G. Fan, J. Liu and F. Zhao for pre-review and discussions. X. Z. thanks F. Lin for EVPSC tutoring. We acknowledge support from the National Natural Science Foundation of China (NSFC) under grant numbers 11621062, 11772294, U1530402 and 11811530001. X.Z. acknowledges the Advanced Light Source Doctoral Fellowship in Residence Program and Collaborative Postdoctoral Fellowship Program. L.Z. acknowledges support from the Fundamental Research Funds for the Central Universities of China (2018XZZX001-05). L.M. acknowledges support from CDAC and NSF (EAR-1654687). Z.F., T.H. and X.H. acknowledge support from the National Key Research and Development Program of China (2016YFB0700400). This research used the resources of the Advanced Light Source, which is a DOE Office of Science User Facility under contract number DE-AC02-05CH11231 and the Shanghai Synchrotron Radiation Facility. This research was

partially supported by COMPRES, the Consortium for Materials Properties Research in Earth Sciences under NSF Cooperative Agreement EAR 1606856.

Author contributions B.C. conceived the project. X.H. directed the TEM examinations. J.X., H.D., H.Z. and K.L. performed the nanocrystal synthesis. X.Z., B.C., L.M., J.Y., N.T. and M.K. performed the high-pressure XRD experiments. Z.F., Y.W., D.A.H., T.H. and X.H. performed the TEM experiments and analysis. L.Z., H.S., Q.L. and Y.M. performed the computational and molecular dynamics simulations. X.Z. and L.M. performed the EVPSC modelling. X.Z. and B.C. wrote the manuscript. All authors discussed the results and commented on the manuscript.

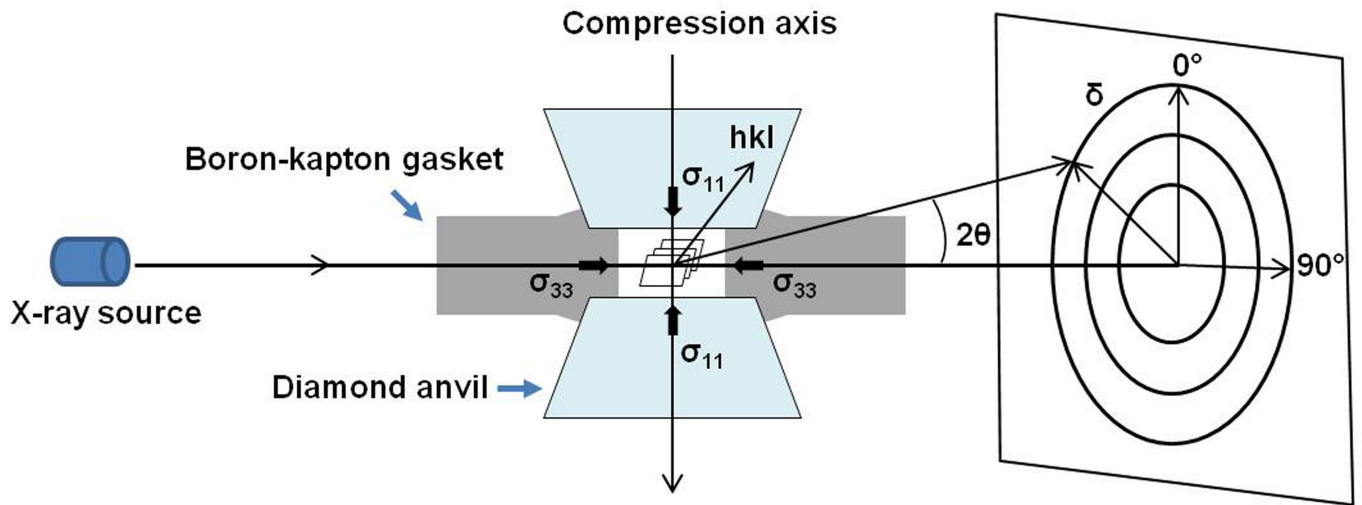
Competing interests The authors declare no competing interests.

Additional information

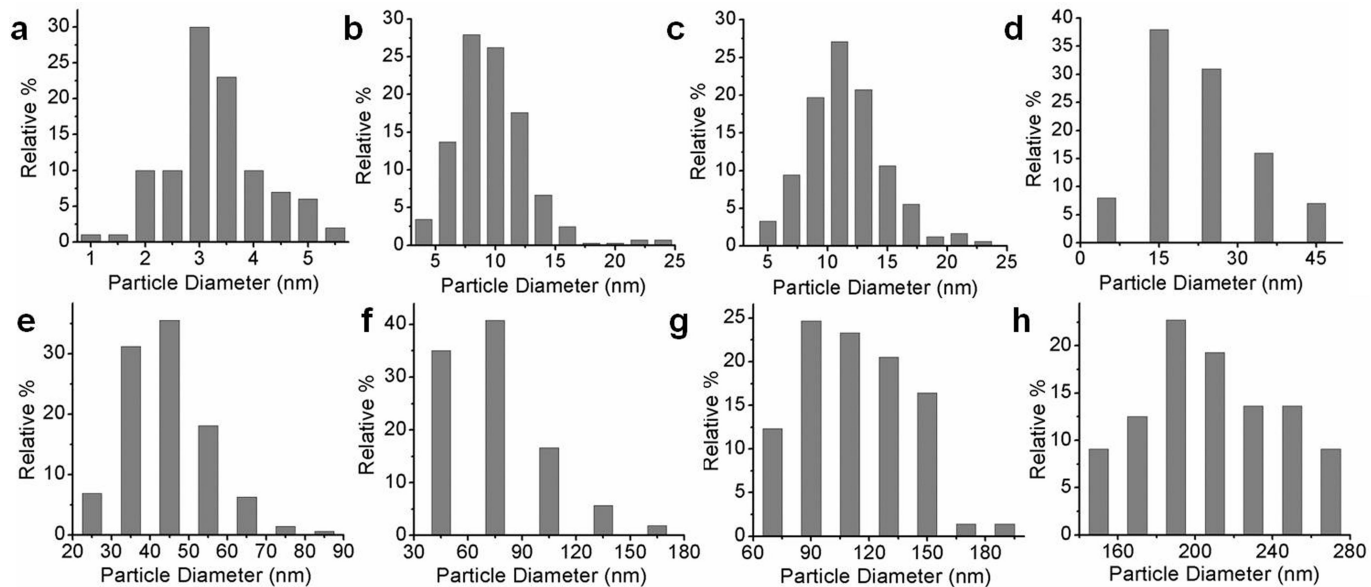
Supplementary information is available for this paper at <https://doi.org/10.1038/s41586-020-2036-z>.

Correspondence and requests for materials should be addressed to X.H. or B.C.

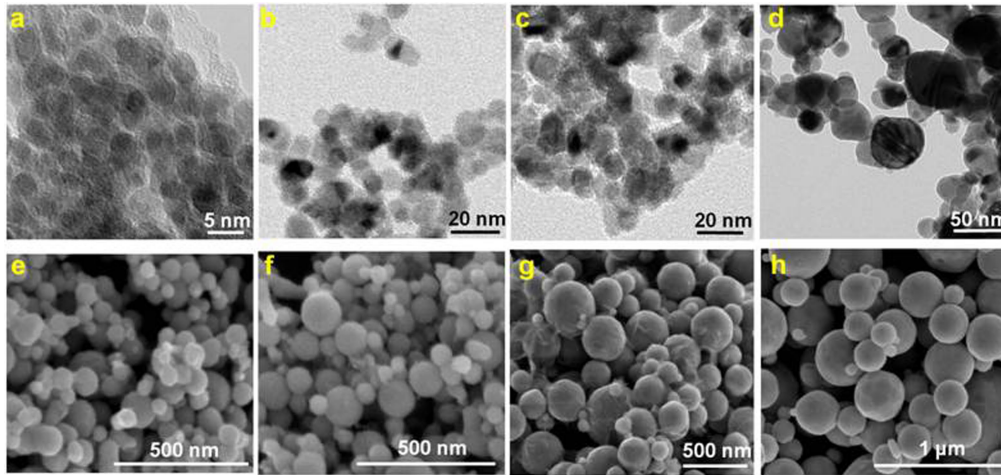
Reprints and permissions information is available at <http://www.nature.com/reprints>.



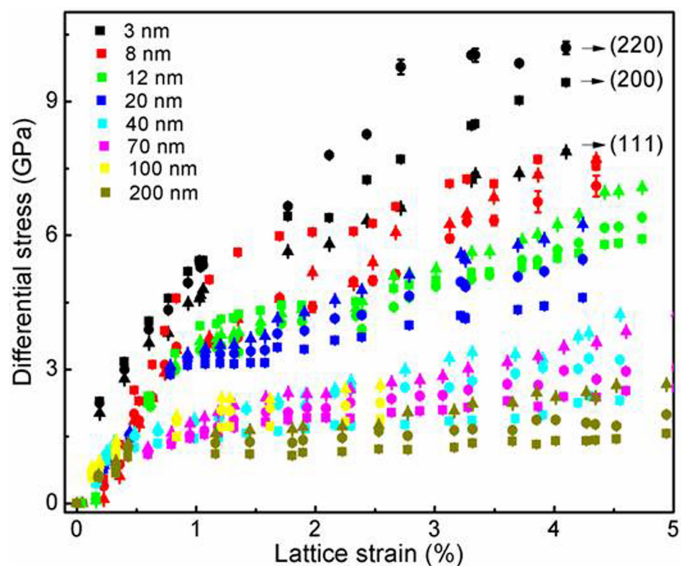
Extended Data Fig. 1 | The experimental setup of radial DAC XRD. Kapton is a polyimide film. hkl represents the lattice planes; δ is the azimuthal angle; and θ represents the diffraction angle.



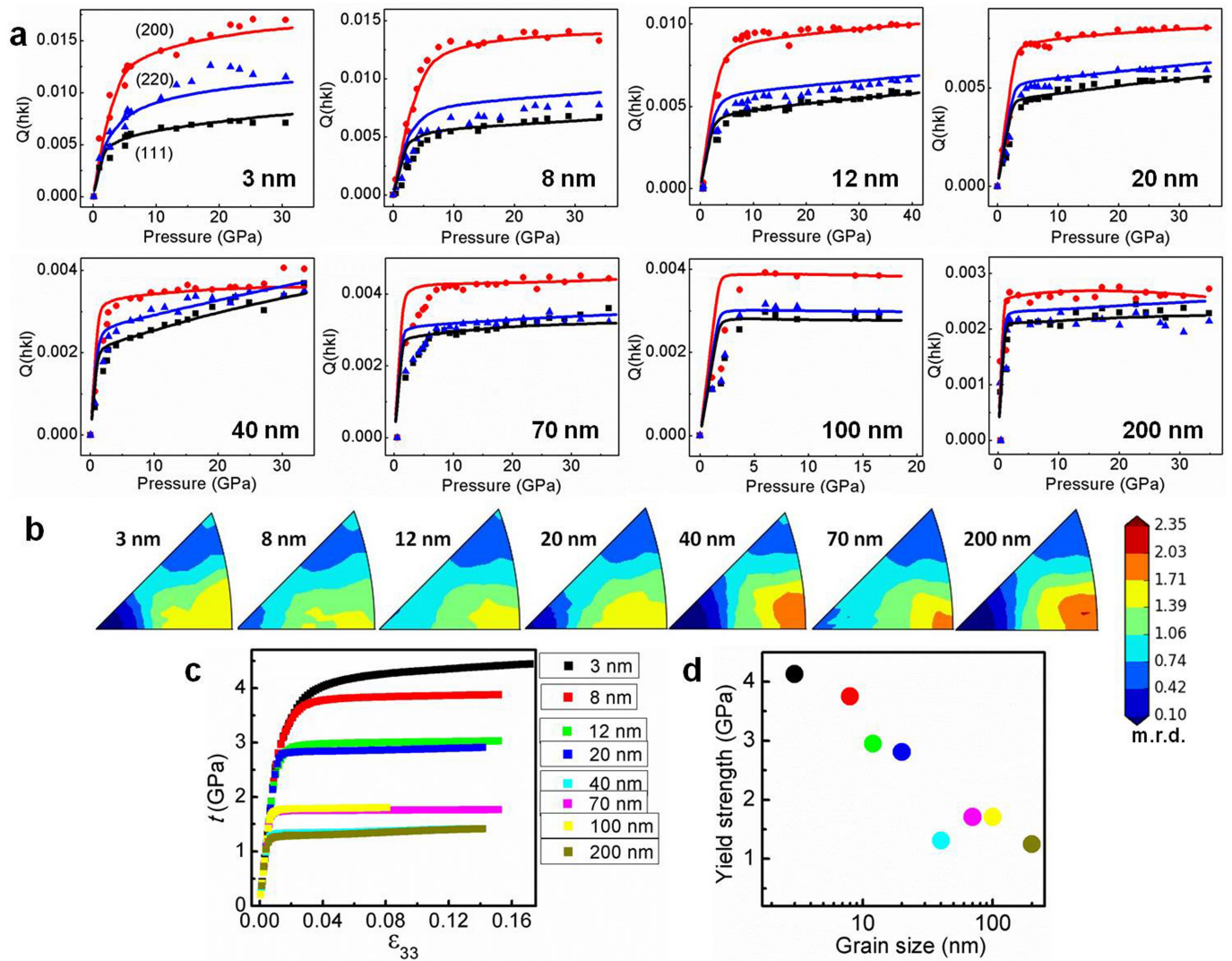
Extended Data Fig. 2 | Grain size distribution of nickel samples. a-d, Grain size distributions in 3-nm, 8-nm, 12-nm and 20-nm nickel; **e-h**, Grain size distribution of 40-nm, 70-nm, 100-nm and 200-nm nickel. The particle sizes of the nickel samples were re-checked with XRD characterization.



Extended Data Fig. 3 | Raw powder samples. a–d, TEM images of raw powder samples of 3 nm (a), 8 nm (b), 12 nm (c) and 20 nm (d) nickel powder before compression. **e–h**, Scanning electron microscopy characterization of 40 nm (e), 70 nm (f), 100 nm (g) and 200 nm (h) nickel powder before compression.



Extended Data Fig. 4 | Plot of differential stress versus hydrostatic lattice strain in the nickel of various grain sizes. The circles, squares and triangles represent (220), (200) and (111) lattice planes, respectively. Strong strength anisotropy is exhibited for different lattice planes, especially at smaller grain sizes. The lattice strain is calculated from the relative change in the unit cell parameter at a given applied stress to the unit cell parameter under ambient pressure (see Supplementary Information). The error bars for differential stress is calculated based on the error of deviatoric strain $Q(hkl)$ and equations (6) to (9). Note that for some of the data points the error bars (see Supplementary Information for definition) are smaller than the sizes of symbols.



Extended Data Fig. 5 | EVPSC modelling results of nickel. **a**, Comparison between simulated $Q(hkl)$ curves versus pressure and measured $Q(hkl)$ values (solid symbols) obtained from experiments. **b**, Simulated texture of nickel at the highest strain (pressure). **c**, Simulated differential stress of nickel versus

plastic strain during zero pressure compression. **d**, Extrapolated yield strength of nickel at ambient conditions without GB sliding. The size-strengthening trend is consistent with that shown in Fig. 1b, although the strength of 40-nm-grain-size nickel obtained with EVPSC is slightly lower.